

Investigation of Operating Parameters' Effects on Bubble Characteristics in a Co-Current Downflow Bubble Column

Meshram, Rohit Buddham^{*}; Yenni, Usha**

CSIR- National Metallurgical Laboratory (NML), Jamshedpur- 831007, INDIA

Kundu, Gautam; Mukherje, Dibyendu

[#]Chemical Engineering Department, Indian Institute of Technology (IIT) Kharagpur- 721302, INDIA

ABSTRACT: Bubble columns are frequently employed as multiphase reactors and gas-liquid contactors. In the bubble column, gas is dispersed into the liquid phase. The dispersion of gas into a liquid is the function of bubble size and its distribution. It also includes the complex process of coalescence and the break up of bubbles. The present research intends to examine the operating parameters' effect, including temperature on bubble characteristics in the ejector-induced downflow bubble column (i. d. 0.05 m X 1.6 m height) via Computational Fluid Dynamics (CFD) and experimental methods. Bubbles inside the column are analyzed and mean bubble diameters are obtained using a photographic technique. The effect of superficial gas velocity (4.25×10^{-3} - 9.68×10^{-3} m/s) and liquid velocity (8.5×10^{-2} - 14.11×10^{-2} m/s) on an average Sauter diameter is studied. The gas holdup variation with temperature (60-80 °C) is also examined. The temperature distribution at different axial locations (0.48-1.35 m) from the top of the column is observed using the CFD model. An empirical model for predicting the temperature, i.e., $Tr (T/Tset)$, is proposed as a function of the Prandtl number, Weber number, Reynolds number, and Froude number.

KEYWORDS: Downflow bubble column; Bubble size; Interfacial area; Temperature; CFD.

INTRODUCTION

Bubble columns are widely used as multiphase reactors in chemical, petrochemical, pharmaceutical, and mining industries because of their simple construction and simplicity of operation. Effectiveness, energy efficiency, and no moving parts offer more advantages to bubble columns over the conventional stirred-tank reactors; however, the design and scale-up of these reactors is still a difficult task. Generally, bubble columns are operated

in co-current, counter-current, and batch modes. The downflow bubble columns offer advantages in terms of higher gas residence time as well as higher interfacial area over the upflow bubble column [1].

The gas-liquid interface plays a crucial role in the proper functioning of bubble column reactors; however, it essentially depends on the bubble size, number of bubbles, and their distribution. Therefore, detailed information

* To whom correspondence should be addressed.

+ E-mail: rohitmeshramiit@gmail.com

1021-9986/2022/10/3426-3435

10/\$/6.00

on these factors in a two-phase ejector-induced downflow bubble column would be of considerable interest.

Numerous authors investigated the bubble characterization in bubble columns using chemical and physical methods. *Vázquez* (2000) described means of measuring the local interfacial area using three chemical methods: the Danckwerts, the Sodium Sulfite, and the Sodium Dithionite. *Ghiassi et al.* (2012) used the light transmission method to estimate the interfacial area in gas-liquid two-phase. The interfacial area is expressed in terms of gas holdup and bubble diameter [4].

The specific interfacial area (a) calculated using the physical method by estimating the gas holdup (ε_g) as,

$$a = \frac{6 \varepsilon_g}{d_s} \quad (1)$$

The average Sauter diameter (d_s) in the above equation is calculated by,

$$d_s = \frac{\sum_{N=1}^{N_i} N_i d_{bi}^3}{\sum_{N=1}^{N_i} N_i d_{bi}^2} \quad (2)$$

where N_i is the number of bubbles.

d_{bi} is the diameter of the bubble.

The gas holdup and bubble diameter are measured by various methods. *Kanaris et al.* (2018) developed a correlation to calculate the Sauter mean diameter and gas holdup in the column. *Youssef A. and Al-Dahhan M.* (2009) reported that the fluid dynamics of the bubble columns were dependent on the internals and process parameters. *Tao et al.* (2019) used the dynamic gas disengagement method to classify large and small bubbles. *Jha et al.* (2008) estimated the local gas holdup in a bubble column provided porous spargers with additives.

Tran et al. (2019) developed the gas-liquid Eulerian Computational Fluid Dynamics (CFD) code to study hydrodynamics under elevated pressure. In the homogeneous bubbly flow regime, it is possible to forecast both the total gas holdup and the mean bubble size. *Patel et al.* (2016) studied three different sets of nozzles inside the jet ejector for the Cl_2 -NaOH system using the population balance approach of numerical simulations. Gas volume fractions, bubble size distributions, and numerical densities of different bubble size groups were predicted and verified with experimental results. *Mutharasu et al.* (2018) investigated flow characteristics in a downflow bubble

column using the 3D Euler-Euler CFD model. Researchers proved that the column could produce up to 54% gas holdup of microbubbles (300–800 μm) experimentally as well as through simulation. *Saad et al.* (2018) investigated air-water flow patterns in a bubble column experimentally and using CFD at an ambient temperature. An electro-conductivity probe was employed to measure the bubble characteristics and effects of gas velocities and locations.

The objective of the current study is to analyse the effect of operating parameters, including temperature on the bubble characteristics experimentally and verify it using CFD simulations.

EXPERIMENTAL SECTION

The experimental setup shown in Fig. 1 consists of a contactor of internal dia. 0.05 m and height 1.6 m. Due to the vacuum formation, water flows from the top through the jet ejector, which carries the air with it. The gas flowmeter and rotameter are used to monitor the flow rate of air and water, respectively. The temperatures along the axial positions are measured via J-type thermocouples connected to a data recorder (NI USB-6210). The total pressure is obtained from the corresponding manometer through PVC tubes. To minimize heat loss, the contactor area is adequately insulated with asbestos. The water is heated in a heater, and its setting and controls are indicated digitally. The experimental setup and procedures are followed according to the earlier method [13].

The gas holdup is measured using U-tube manometers by the "flow isolation technique" [14, 15]. Several techniques are accessible for calculating bubble size measurements, as discussed in the introduction. The photographic method is adopted in the current study as it is very simple and convenient. The gas-liquid dispersion may be observed through the transparent-view glass fitted on the contactor.

Numerical simulation methodology

CFD studies are implemented on a multiphase mixture model with dispersed phases of air and water. Numerical simulation is performed for heat transfer studies to attain the temperature distribution in the column with the assumption that the column is filled with water. Thus water volume fraction is patched as 1. Air, water and hot water (80 °C) is flowing in and out as specified in Fig. 2.



Fig. 1: Image of an experimental set-up.

Downflow bubble column geometry is designed as shown in Fig. 2 and is exported to Fluent™ for numerical studies. Grid independence study is performed by reducing the maximum face size in the mesh definition. The optimized mesh has 480008 nodes with 0.45 orthogonal quality.

An implicit scheme is used for time discretization using a first-order upwind interpolation scheme for volume fraction. Interpolation schemes utilized for pressure, momentum, and energy are PRESTO, QUICK and first-order upwind, respectively.

The pressure-velocity coupling method is used in the numerical outline. Boundary conditions are considered within the experimental range with a velocity inlet of superficial gas velocity of 6×10^{-3} m/s, liquid velocity inlet of 8.5×10^{-2} m/s and hot water velocity inlet of 1 m/s at 80 °C. The transient study is performed with time step size of 5×10^{-3} s and convergence criteria are monitored by specifying equation for each residual component in the range of 10^{-4} . The temperature distribution at different axial locations

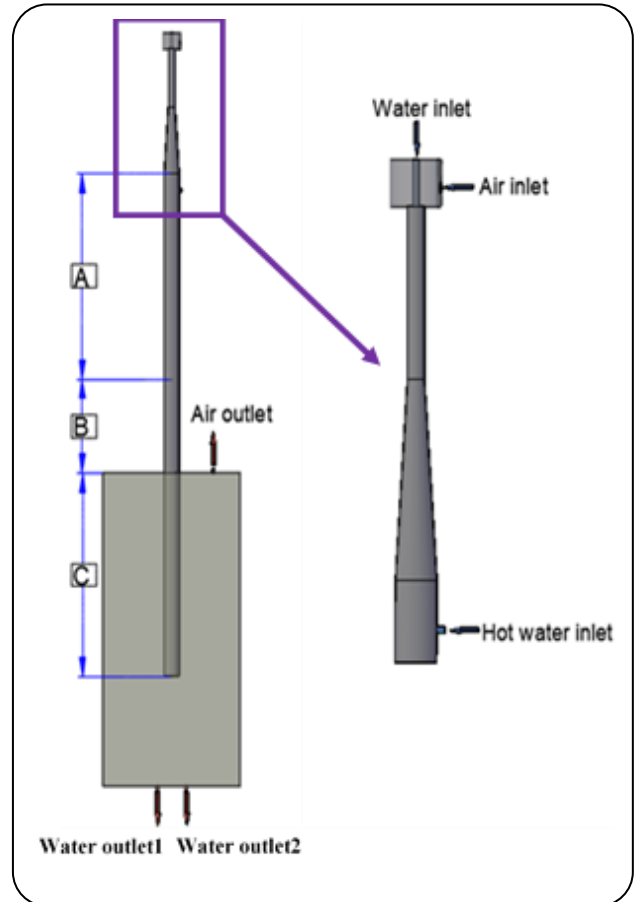


Fig. 2: CAD model of the downflow bubble column.

(0.48-1.35 m) from the top of the column is observed.

The energy equation for computing temperature distribution is given by,

$$\frac{\partial}{\partial t} \sum (\alpha_N \rho_N E_N) + \nabla \cdot \sum (\alpha_N v_N (\rho_N E_N + p)) = \nabla \cdot (k_{\text{eff}} \nabla T) \quad (3)$$

Where α_N is the volume fraction of phase N such that

$$\alpha_N = \frac{Q_N}{\sum_N Q_N} \quad (4)$$

k_{eff} is the effective thermal conductivity such that

$$k_{\text{eff}} = \sum (k_N + k_t) \quad (5)$$

Wherein k_t is the turbulent thermal conductivity is defined by the standard k - ϵ turbulence model and is given by

$$k_t = \frac{c_p \mu_t}{Pr_t} \quad (6)$$

Bubble size measurement

In the present work, bubble characteristics are analysed using the photographic method. A Sony (14.1 Megapixel optical steady shot DSC – W 380) zoom (5X) digital video camera is employed for the recording of images. These images are used to measure bubble size by analysing the coalescence/breakage mechanisms.

Images are captured at steady-state flow conditions by positioning the camera at approximately 35 cm away from the contactor. The digital photographs are processed and analysed using Image Pro-Plus 6.0 software. Overlapped bubbles as one big bubble are eliminated consistently from the measurements [16]. The photos are taken at different operating conditions at three axial positions namely A, B, and C as shown in Fig. 3-6. During experiments, 3 to 4 pictures are taken for each operating condition and location to minimize the error. The quality of the images is enhanced by regulating the contrast. In order to measure the bubble size by the software and to distinguish between bubbles and background, a threshold criterion is used. The grey scale is maintained at 8 [17].

The calibration for the pixel is as follows:

1:300

So, 10 mm = 300 pixels

$10/300 = 0.0333$ mm per pixel

The images are processed in software to calculate maximum and minimum axes which approximated the bubbles as spheroids [18]. The third dimension is computed assuming that the bubbles are symmetric around the minimum axes.

$$d_{be} = \sqrt[3]{(d_{b,max}^2 d_{b,min})} \quad (7)$$

Where $d_{b,max}$ is the maximum bubble diameter.

and $d_{b,min}$ is the minimum bubble diameter of the bubble.

RESULTS AND DISCUSSION

The diameter of the contactor is 0.05 m; hence the radial distribution is neglected in the present study.



Fig. 3: Image at section B, 600 LPH.

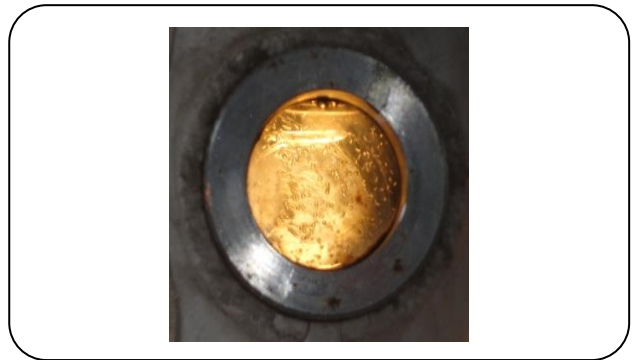


Fig. 4: Image at section B, 800 LPH.

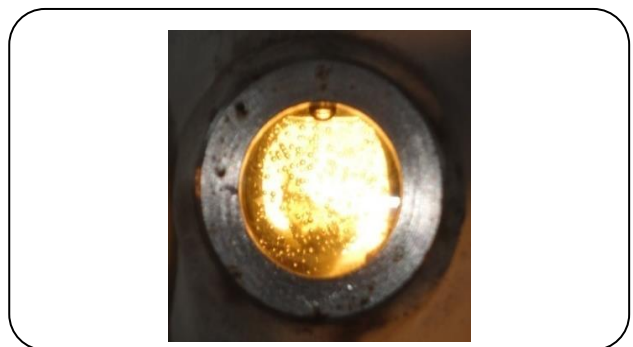


Fig. 5: Image at section C, 600 LPH.

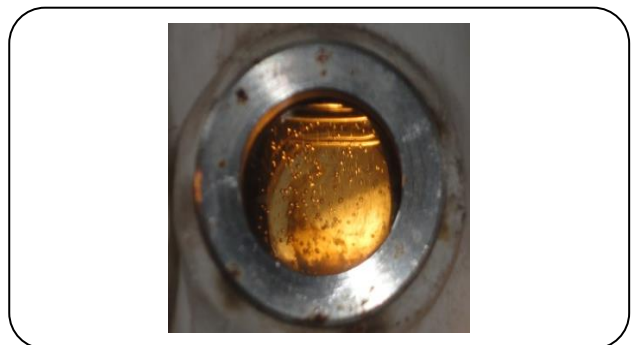


Fig. 6: Image at section C, 800 LPH.

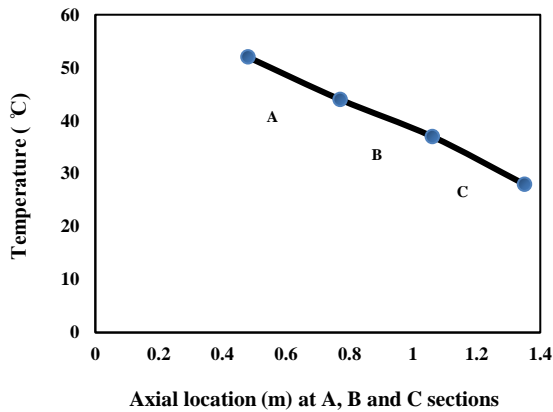


Fig. 7: Temperature variation along the axial sections.

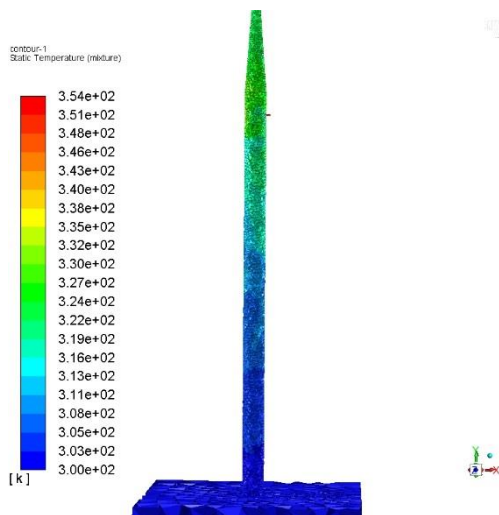
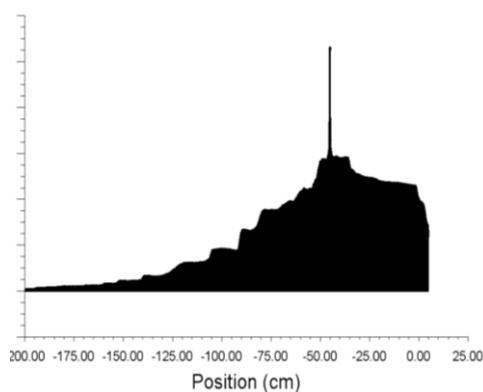


Fig. 8: Temperature contour along the axial direction.

Temperature variation with axial location

The transient study is performed using CFD and the temperature at each axial section A (0.48 to 0.77 m), B (0.77 to 1.06 m) and C (1.06 to 1.35 m) from the top of the column are shown in Fig. 7 and 8.

From the temperature distribution contour, it is observed that the temperature is reducing in an axial downward direction of the bubble column due to convective flow of water in the downward movement of gravity. This leads to the thermal gradient at different axial sections. For constant liquid velocity, gas velocity and hot water temperature, temperature gradient is obtained along the axial direction as shown in Fig. 8. The temperature gradient would help to understand the different interfacial area obtained across the bubble column at different sections as shown in Fig. 13. It is observed that Section B has maximum interfacial area compared to Section A and C. Ideally, viscosity and surface tension are less at elevated temperature and so section A would have enhanced bubble-bubble interactions, the bubble collision, and coalescence phenomenon. However, the bubble number flux is observed to be maximum at Section A rather than at Section B and minimum at Section C, as shown in Fig. 12. The combined effects of temperature and bubble number flux offer maximum interfacial area at Section B. Section C has the least interfacial area and bubble number flux due to minimum temperature distribution.

Average Sauter diameter deviation with axial location

The average Sauter diameter decreases for all operating temperatures along the axial length as illustrated in Fig. 9. The superficial liquid velocities varied between 8.5×10^{-2} – 14.11×10^{-2} m/s and superficial gas velocities varied between 4.25×10^{-3} – 9.68×10^{-3} m/s. It appears that the bubble size in Sections A and B are more significant than Section C. Due to the liquid jet force, larger bubbles generated in Section A are broken up into small bubbles and are carried downward to Sections B and C. Simultaneously, fine bubbles go up to Sections A and B due to buoyancy and result in the substantial average Sauter diameter of Sections A and B compared to Section C.

Average Sauter diameter at different liquid velocity, gas velocity, and temperature

Gas holdup and gas void fraction increase with superficial gas velocity. Gas holdup (ϵ_g) is strongly related to air bubble diameter and is determined by the Sauter mean diameter. Large bubbles have higher rise velocity than small bubbles; therefore, it is expected that the residence time of large bubbles decreases and causes gas holdup to fall. When compared to an up-flow system, gas bubbles move against their high buoyant force,

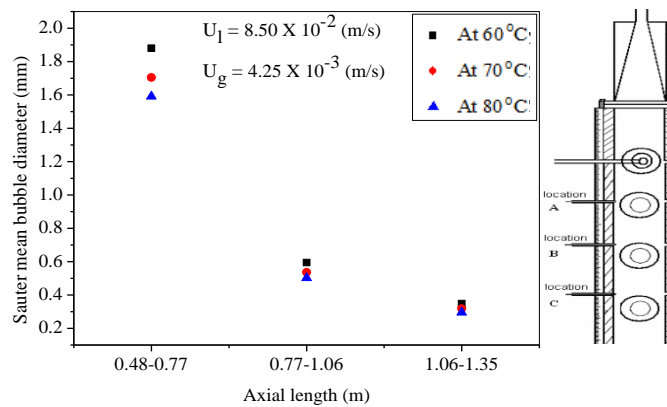


Fig. 9: Average Sauter diameter at different temperatures along axial locations [Sections A (0.48-0.77m), B (0.77-1.06 m) and C (1.06-1.35 m)].

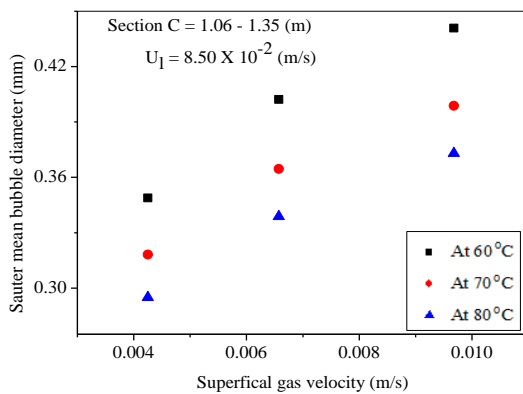


Fig. 10: Variation of average Sauter diameter with various superficial gas velocities at different temperatures in Section C (1.06-1.35 m).

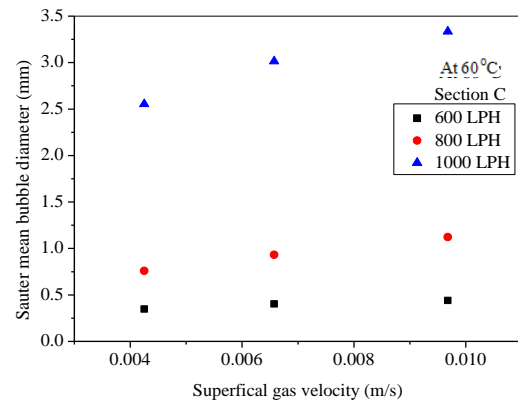


Fig. 11: Variation of average Sauter diameter with different superficial gas velocities and liquid velocities at a constant temperature of 60°C in Section C.

resulting in a higher slip velocity. Accordingly, the bubbles have a longer residence time and provide a greater gas holdup [19].

The bubble size distribution varies with the superficial gas velocity, which enhances bubble-bubble interactions. As per Fig. 10 and 11, it is seen that the average Sauter diameter increases with superficial gas velocity. With rising gas velocity, bubble collision and the coalescence phenomenon increase, resulting in increased Sauter mean bubble diameter [20, 21].

However, the reverse situation is observed with increasing liquid velocity. The turbulence level increases with liquid velocity and leads to smaller bubble sizes [22]. The fine bubbles are found at Section C (1.06-1.35 m) of the column which are carried in downward direction by the liquid flow.

Bubble number flux along the axial length

The bubble number flux is the result of growth in bubble size. It increases in Sections C and B over Section A. A high liquid flow rate results in increasing collision frequency between bubbles. The fine bubbles of Section C go up and accumulate in Sections A and B due to buoyancy. This also results in different bubble number flux in various locations. The typical increasing profile of bubble number flux with the axial location is shown in Fig. 12.

Interfacial area at different gas velocity

Generally, the interfacial area depends on the physical and chemical properties of the fluid and hydrodynamics. The experimental result revealed that the interfacial area increases with superficial gas velocity as shown in Fig. 13.

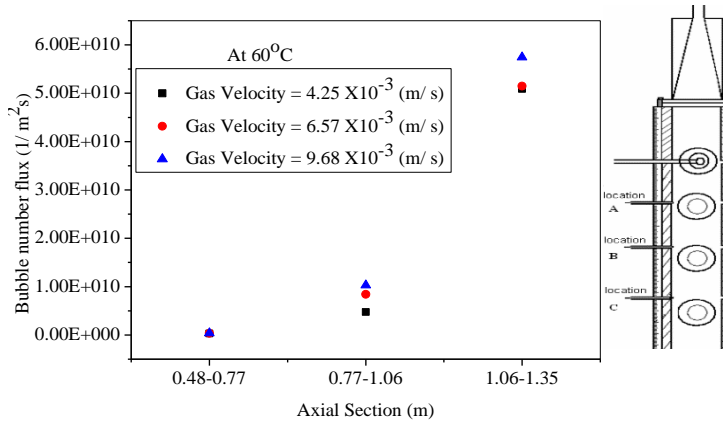


Fig. 12: Variation of bubble number flux with a different axial section at different superficial gas velocities at 60°C.

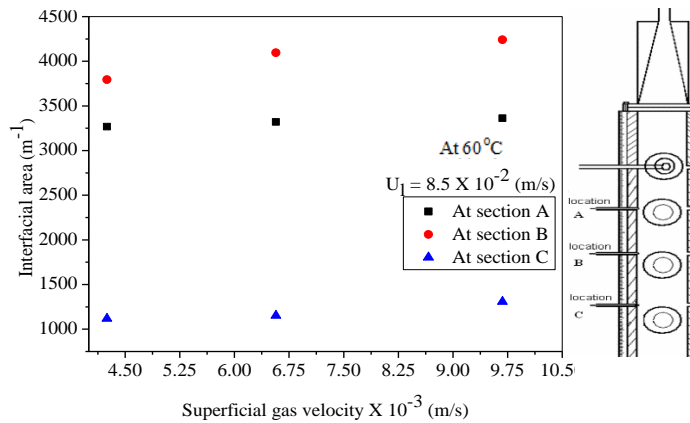


Fig. 13: Variation of an interfacial area with superficial gas velocity in different sections of the column.

The specific interfacial area varies with the average Sauter diameter due to the coalescence effect at various axial locations. Gas holdup changes due to bubble number flux as well as temperature effects. Wu *et al.* (2016) also observed a similar changing trend for bubble diameter, gas holdup, and the interfacial area to increase gas velocity.

Gas holdup dependence on temperature

The bubble size is dependent on gas density, liquid viscosity, and surface tension [23]. Fig. 14 shows the influence of superficial gas velocity and liquid velocity on gas holdup at different temperatures. A higher gas throughput generally helps to increase gas holdup [24]. The increase in gas density increases the interstitial force in the bubble, favoring bubble breakage. The reduction in liquid viscosity and surface tension leads to a small bubble diameter.

Statistical analysis

The dimensionless model is developed to correlate temperature with superficial gas velocities, liquid velocities, average Sauter diameter, column diameter, and other physical properties. The experimental data can be analysed by expressing a temperature ratio, T_r (T/T_{set}).

The temperature ratio is the function of:

$$T_r \propto (U_l, \rho_l, \mu_l, D_c, d_s, k_l, C_{pl}, U_g, \sigma_l, \varepsilon_g, g) \quad (8)$$

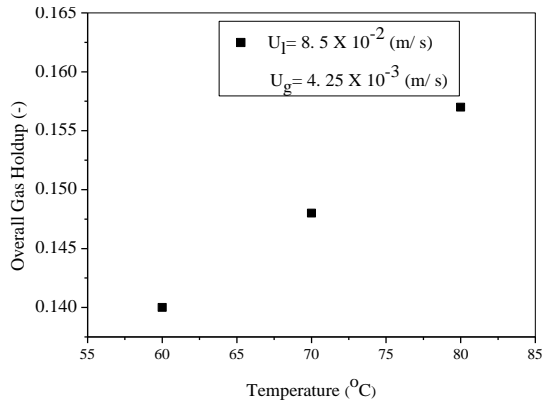
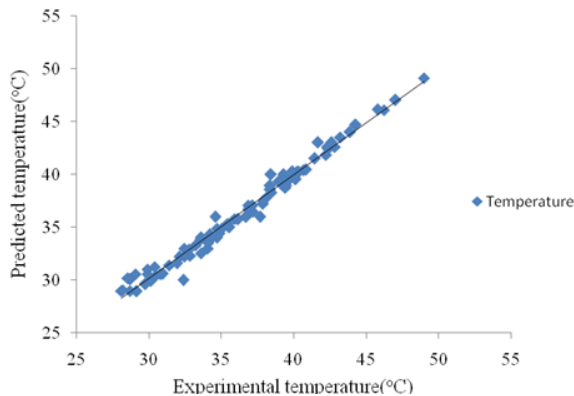
By the Rayleigh method of dimensionless analysis following correlation presented-

$$T_r = \text{constant} (\text{Re})^{-k_1} (\text{Re} * \text{Pr})^{k_2} (\text{Fr})^{-k_3} (\text{We})^{-k_4} \left(\frac{U_l}{U_g}\right)^{k_5} \left(\frac{d_s}{D_c}\right)^{k_6} (\varepsilon_g)^{k_7} \quad (9)$$

This relation is solved by multiple regression analysis using the experimental data. A generalized correlation

Table 1: Regression statistic for temperature ratio.

Regression Statistics	
Multiple R	0.975268
R Square	0.951147
Adjusted R Square	0.946463
Standard Error	0.017994

**Fig. 14: Variation of overall gas holdup with the temperature at constant superficial gas and liquid velocity.****Fig. 15: Predicted temperature ratio based on proposed model versus experimental temperature ratio for average Sauter diameter.**

for temperature ratio depending on column diameter, superficial gas velocity, and average Sauter diameter for the air-water system is obtained as-

$$T_r = 0.0148 (Re)^{-0.0156} (Pr)^{0.012153} (Fr)^{0.315658} (We)^{-0.00898} \left(\frac{U_l}{U_g}\right)^{-0.49162} \left(\frac{d_s}{D_c}\right)^{0.049683} (\varepsilon_g)^{-0.01326} \quad (10)$$

The regression statistic for temperature ratio (T_r) is shown in Table 1.

The predicted temperature ratio based on the proposed model shows acceptable agreement with experimental results as shown in Fig. 15.

The above correlation has limitations with the following experimental data,

$$\text{where, the ranges are } 8.50 \times 10^{-2} \leq U_l \leq 14.11 \times 10^{-2} \text{ m/s} \\ 4.25 \times 10^{-3} \leq U_g \leq 9.58 \times 10^{-3} \text{ m/s} \\ 0.295 \leq d_s \leq 5.289 \text{ mm, and } D_c = 0.05 \text{ m}$$

CONCLUSIONS

In the present study, the analysis of bubble size in sections A, B, and C of the co-current downflow bubble column (i.d.= 0.05m x height= 1.6 m) and the influence of temperature, superficial liquid and gas velocities on the bubble characteristics are proposed. The bubble diameter measurement is accomplished using the photographic technique. The liquid jet energy dissipates at the top of the column, resulting in the breaking of the large bubbles and movement of smaller bubbles downward. The overall average Sauter diameter is obtained in the range of 0.295-5.289 mm. The smaller bubble size results in a larger interfacial area. Temperature affects properties of both gas as well as liquid and eventually bubble size. Downflow bubble column geometry is designed and is exported to FluentTM for numerical studies. The temperature distribution at different axial locations (0.48-1.35 m) from the top of the column is observed. An empirical correlation for the prediction of the temperature as a function of dimensionless numbers, including the Weber number, Reynolds number, the Prandtl number, and the Froude number has been proposed, which agrees with experimental results.

Acknowledgments

This research work was supported by the Chemical Engineering Department, Indian Institute of Technology, Kharagpur, India.

Nomenclature

a	Interfacial area, m^{-1}
C_{pl}	Specific heat of liquid, $J/kg \text{ } ^\circ C$
d_b	Diameter of bubble, m
d_{be}	Equivalent spherical bubble diameter, m
D_c	Diameter of column, m
d_s	Average Sauter diameter or Sauter mean bubble diameter, m

Fr	Froude number based on superficial gas velocity	$\frac{U_g^2}{gD_c}$ (-)
g	Acceleration due to gravity, m/s ²	
k ₁ to k ₇	Constant	
k _l	Thermal conductivity of liquid, W/m °C	
Pr	Prandtl number of liquid	$\frac{C_{p,l} \mu_l}{k_l}$ (-)
Re	Reynolds number based on superficial gas velocity	$\frac{D_c U_g \rho_l}{\mu_l}$ (-)
T	Recorded temperature from Labview software	
T _r	Temperature ratio, T/Tset	
Tset	Heating bath temperature	
U _g	Superficial gas velocity, m/s	
U _l	Superficial liquid velocity, m/s	
We	Weber number based on superficial gas velocity	$\frac{\rho_l D_c U_g^2}{\sigma_l}$ (-)

Greek Letters

ε _g	Gas holdup (-)
μ _l	Viscosity of liquid, kg/m s
ρ _l	Density of liquid, kg/m ³
σ _l	Surface tension of liquid, kg/s ²

Received : Jul 15, 2021 ; Accepted : Nov. 29, 2021

REFERENCES

- [1] Kalaga D., Ansari M., Turney D., Hernandez-Alvarado F., Kleinbart S., Arun Kumar K., Joshi J., Banerjee S., Kawaji M.; [Scale-up of a Downflow Bubble Column: Experimental Investigations](#), *Chem. Eng. J.*, **386**: 121447 (2020).
- [2] Vázquez G., Cancela M., Riverol C., Alvarez E., Navaza J.; [Determination of Interfacial Areas in a Bubble Column by Different Chemical Methods](#), *Ind. Eng. Chem. Res.*, **39(7)**: 2541-2547 (2000).
- [3] Ghiassi S., Safekordi A., Babazadeh Shareh F.; [Determination of Interfacial Area in Gas-Liquid Two-Phase by Light Transmission](#), *Iran. J. Chem. Chem. Eng. (IJCCE)*, **31(1)**: 81-87 (2012).
- [4] Majumder S.; "Hydrodynamics and Transport Processes of Inverse Bubbly Flow", Netherlands: Elsevier Science (2016).
- [5] Kanaris A., Pavlidis T., Chatzidafni A., Mouza A.; [The Effects of the Properties of Gases on the Design of Bubble Columns with a Fine Pore Sparger](#), *Chem. Eng.*, **2(1)**:11 (2018).
- [6] Youssef A., Al-Dahhan M., Impact of Internals on the Gas Holdup and Bubble Properties of a Bubble Column, *Ind. Eng. Chem. Res.*, **48(17)**: 8007-8013 (2009).
- [7] Tao F., Ning S., Zhang B., Jin H., He G.; [Simulation Study on Gas Holdup of Large and Small Bubbles in a High Pressure Gas-Liquid Bubble Column](#), *Processes*, **7(9)**: 594 (2019).
- [8] Jha A., Raj Mohan B., Chakraborty S., Meikap, B.; [Studies on Gas Holdup in a Bubble Column Using Porous Spargers with Additives](#), *Asia-Pacific J. of Chem. Eng.*, **3(4)**: 417-424 (2008).
- [9] Tran B., Nguyen D., Ngo S., Lim Y., Kim B., Lee D., Go K., Nho N.; [Hydrodynamics and Simulation of Air-Water Homogeneous Bubble Column Under Elevated Pressure](#), *AIChE J.*, **65(10)**: e16685 (2019).
- [10] Patel D., Chaudhari A., Laari A., Heilio M., Hamalainen J. and Agrawal K., [Numerical Simulation of Bubble Coalescence and Break-Up in Multinozzle Jet Ejector](#), *J. Appl. Math.*, Article ID 5238737: 1-19 (2016).
- [11] Mutharasu L.C., Kalaga D.V., Sathe M., Turney D.E., Griffin D., Li X., Kawaji M., Nandakumar K., Joshi J.B., [Experimental Study and CFD Simulation of the Multiphase Flow Conditions Encountered in a Novel Down-Flow Bubble Column](#), *Chem. Eng. J.*, **350**: 507-522 (2018).
- [12] Saad N.S., Ahmed A. Mohammed, Farah K. Al-Jubory, Shahzad Barghi; [CFD Assessment of Uniform Bubbly Flow in a Bubble Column](#), *J. Pet. Sci. Eng.*, **161**: 96-107 (2018).
- [13] Meshram R. B., Kundu G., Mukherjee D.; [Heat Transfer Studies in Ejector-Induced Downflow Bubble Column](#), *Int. J. Chem. React. Eng.*, **14(5)**: 955-964 (2016).
- [14] Kundu G., Mukherjee D., Mitra A. K., [Experimental Studies on a Concurrent Gas-Liquid Downflow Bubble Column](#), *Int. J. Multiph. Flow*, **21**: 893-906 (1995).
- [15] Mandal A., Kundu G., Mukherjee D., [Gas-Holdup Distribution and Energy Dissipation in an Ejector Induced Downflow Bubble Column: The Case of Non-Newtonian Liquid](#), *Chem. Eng. Sci.*, **59**: 2705-2713 (2004).

- [16] Majumder S. K., Kundu G., Mukherjee D., [Bubble Size Distribution and Gas-Liquid Interfacial Area in a Modified Downflow Bubble Column](#), *Chem. Eng. J.*, **122** (1-2) : 1-10 (2006).
- [17] Beth J., Walter M., Branson D., Michael L., Michael Pm, [Feasibility of an in Situ Measurement Device for Bubble Size and Distribution](#), *Bioprocess Biosyst Eng.*, **30**(5): 313-326 (2007).
- [18] Polli M., Di Stanislao M., Bagatin R., Abu Bakr E., Masi M., [Bubble Size Distribution in the Sparger Region of Bubble Columns](#), *Chem. Eng. Sci.*, **57**: 197-205 (2002).
- [19] Mandal A., [Characterization of Gas-Liquid Parameters in a Down-Flow Jet Loop Bubble Column](#), *Braz. J. Chem. Eng.*, **27**(02): 253 – 264 (2010).
- [20] Wu X., Li H., He L., Wu W., [Numerical Prediction of Bubble Size and Interfacial Area Concentration in the Liquid Bath of Entrained-Flow Coal Gasifier](#), *Braz. J. Chem. Eng.*, **33**(01): 203-214 (2016).
- [21] Camacho O., Gutiérrez-Rojas M., Torrez-Martínez D., Lizardi-Jiménez M., [Gas Hold Up in the Cultivation of a Petroleum-Degrading Bacterial Consortium](#), *Environ. Eng. Manag. J.*, **17**(5): 1209-1216 (2018).
- [22] Hernandez-Alvarado Freddy, Kalaga Dinesh V., Turney Damon, Banerjee Sanjoy, Joshi Jyeshtharaj B., Kawaji Masahiro, [Void Fraction, Bubble Size and Interfacial Area Measurements in Co-Current Downflow Bubble Column Reactor with Microbubble Dispersion](#), *Chem. Eng. Sci.*, **168**: 403-413 (2017).
- [23] Rakoczy R., Masiuk S., [Experimental Study of Bubble Size Distribution in a Liquid Column Exposed to a Rotating Magnetic Field](#), *Chem. Eng. Process.*, **48**(7): 1229-1240 (2009).
- [24] Upadhyay R. K., Kaim J. and Roy S., [Investigation of Downflow Bubble Columns: Experiments and Modeling](#), *J. Chem. Eng. Jpn.*, **42**: 156–161 (Supplement 1) (2009).